

NEED TITLE

SOME PEOPLE

Draft version May 28, 2015

ABSTRACT

write this

Subject headings: diffusion – nuclear reactions – stars: abundances, surface – stars: neutron – X-rays: binaries, bursts

1. INTRODUCTION

The rapid formation of stars remains an unsolved problem in astrophysics.

Here we will focus on the physics of rapid star formation and accretion. An early model of Shu (1977) estimated the accretion rate onto stars by assuming that stars form from hydrostatic cores supported by thermal gas pressure. The accretion rate in his model was independent of time, given by $M = m_0 c_s^3 / G$, where c_s is the sound speed in molecular gas, and $m_0 = 0.975$. Shu (1977) predicted a maximum accretion rate was yr^{-1} , which is too small to explain the origin of massive stars.

Later workers overcame the difficulty with the accretion rate by adopting the turbulence speed in lieu of the sound speed (Myers & Fuller 1992, McLaughlin & Pudritz 1997, McKee & Tan 2003). In doing so they were able to replace the slower signal speed of sound with the faster turbulent speed. However, they rely on assuming that a hydrostatic core supported by turbulent pressure is the initial condition and that turbulence is static and unaffected by the collapse.

Recently Murray & Chang (2015), hereafter MC15, developed a 1-D model of spherical collapse that treat turbulence as a dynamical variable and does not assume that the initial condition is a hydrostatically supported region. They were able to accomplish this by taking advantage of the recent results of Robertson & Goldreich (2012) on compressible turbulence. In particular

need equation

Hence, this allowed MC15 to include an energy equation for the turbulent velocity that alongside the equations for mass continuity and momentum gives a set of equations that can be solved in spherical symmetry numerically. In addition, they were able to analytically show that the results of their calculations gave density and velocity profiles that appear to be in line with both recent numerical calculations (Lee et al 2015) and observations.

In particular, their basic results are that the run of density asymptotes to

$$\rho(r, t) = \begin{cases} \rho(r_0) \left(\frac{r}{r_0}\right)^{-3/2}, & r < r_* \\ \rho(R, t) \left(\frac{r}{R}\right)^{-k_\rho}, & k_\rho \approx 1.6 - 1.8 \quad r > r_* \end{cases} \quad (1)$$

Since k_ρ is fairly close to 1.5 at all radii, taking $r_0 = R$

is a fair approximation. The infall velocity

$$u_r(r, t) = \begin{cases} -\Gamma \sqrt{\frac{GM_*(t)}{r}}, & \sim r^{-1/2} \quad r < r_* \\ -\Gamma \sqrt{\frac{GM(r, t)}{r}}, & \sim r^{0.2} \quad r > r_*, \end{cases} \quad (2)$$

where $\Gamma \approx 0.7$ at small radii, and $\Gamma \approx 1.0$ at large radii.

The turbulent velocity

$$v_T(r, t) = \begin{cases} \frac{1}{2\eta} \Gamma \sqrt{\frac{GM_*(t)}{r}}, & \sim r^{-1/2} \quad r < r_* \\ \frac{1.2}{\eta} \Gamma \sqrt{\frac{GM(r, t)}{r}}, & \sim r^{0.2} \quad r > r_*, \end{cases} \quad (3)$$

The stellar mass increases quadratically with time

$$M_*(t) = \phi M_{\text{cl}} \left(\frac{t - t_*}{\tau_{\text{ff}}} \right)^2. \quad (4)$$

The mass accretion rate

$$\dot{M}(r, t) = \begin{cases} 4\pi R^2 \rho(R) u_r(r, t), & \sim t r^0 \quad r < r_* \\ 4\pi R^2 \rho(R) u_r(r, t) \sim t^0 r^{0.2}, & r > r_*. \end{cases} \quad (5)$$

These results compared favorable with the results of numerical simulations (Lee et al. 2015). However, it is unclear if the results of

2. DETAILED SIMULATIONS OF TURBULENT COLLAPSE

We use the adaptive mesh refinement code FLASH ver. 4.0.1 (Fryxell et al. 2000 ; Dubey et al. 2008) to model isothermal, self-gravitating, hydrodynamic turbulence on isothermal gas with three-dimensional (3D), periodic grids and 8 levels of refinement on a root grid of 128^3 , giving an effective resolution of $32K^3$. Self-gravity is computed with a multi-grid Poisson solver (see Ricker 2008), coupled with a fast-Fourier transform solution on the root grid. Similar to (Lee et. al Feb. 2015) our FLASH runs use the Harten-Lax-van Leer-Contact Riemann solver and an unsplit solver. (**Lee et. al use Lee & Deane (2009) do we?**)

We start with a box with the physical length set to $L = 16\text{pc}$ using periodic boundary conditions. The initial mass density is $\rho = 3 \times 10^{-22}$ and the isothermal, ambient gas is set to a sound speed of $c_s = 2.64 \times 10^4$ **we also set Mach_{ambient} = 5.0 include?**. To initialize our simulations, we drive turbulence by applying a large scale ($1 \leq kL \leq 2$) solenoidal acceleration field as a momentum and energy source term. We apply this field in the

absence of gravity and sink particle formation for 3 dynamical times until a statistical steady state is reached.

WHY JUST SOLENOIDAL

This fully developed turbulent state is the initial condition to which we add self-gravity and sink particle formation for our star formation experiments. Sink particles are formed as described in Lee et al. (2014) and described briefly below.

The gravitational force is computed differently than the gas. Sink particle-sink particle forces are computed via direct N-body calculation. While sink particle-gas and gas-sink particle is computed via the multi-grid Poisson solver. As a result of these additional computations, two large scale gravity solutions must be found per timestep as oppose to one. This allows to avoid the computationally expensive task of computing gas-sink particle forces via direct summation.

We have also implemented a new algorithm for mesh refinement in these simulations. As gas collapse under self gravity, certain regions rapidly increase in density. These regions are refined when the Truelove criterion ($\lambda \leq 4\Delta x$) is met. This corresponds to a condition on the density

$$(6)$$

which when met causes the local grid to be refined by a factor of 2 provided that the maximum refinement level is not reached.

When the Truelove criterion is met at highest refinement level, the excess mass in a cell is transferred either to a newly created sink particle or to a sink particle whose accretion radius includes the cell. This behavior is the same as in Lee et al. (2014), albeit at a much higher resolution. We should also note that like Lee et al. (2014), our sink particle creation prescription is different from the prescription of Federrath et al. (???) where additional checks need to be performed. Our base grid's resolution of 128^3 gives a cell length of 1.2×10^{-1} pc which is sufficient to resolve the Jean's length

$$\lambda_J \equiv \sqrt{\frac{\pi c_s^2}{G \bar{\rho}}} \approx 3.5 \text{ pc} \quad (7)$$

3. NUMERICAL RESULTS

To initialize our simulation, we begin by applying solenoidal stirring forces to the uniform, periodic simulation volume at the root grid resolution of 128^3 until statistical equilibrium is reached (approximately three crossing times). After this equilibrium is established, we then apply self gravity, adaptive mesh refinement, and sink particle creation. In Figure ?? we show a projection along the x-axis of the entire simulation volume that has up to 10 levels of refinement, giving an effective resolution of $128 K^3$. Regions that are highly refined are the densest regions which are smoother than the low-density more pixelated regions.

The high density regions appear to be organized along filaments. These filaments span most of the simulation size, and have a width of 0.5 to 1 pc. Moreover, these filaments appear to flow into large clumps. This is in line with previous work including Lee et al. 2014. These clumpy regions have the highest densities and, hence, are prone to fulfill the criterion for star particle formation.

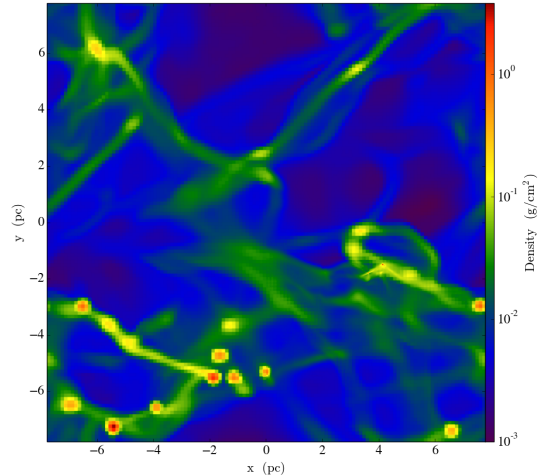


FIG. 1.— Projection of the density along the z-axis of the entire simulation volume. The root grid is 128^3 with up to 8 levels of refinement, giving an effective resolution of $32 K^3$. This snapshot is taken 2.8 Myr after star formation is turned on.

At the instance in time shown in Figure ??, a total of five star particles have been formed. However, these star particles are not formed in isolation. Rather they congregate in two star forming regions shown in Figure ???. In these regions, the sink particles that are formed lay within 0.1 pc of one another, which reflects that the highest density regions are concentrated toward the center. Visually, the character of accretion at the this outer scale appear to flow along filaments, though previous work (Lee et al. 2014) has shown that the majority of accretion is spherical. We discuss this more quantitatively below **INCLUDE A STUDY OF LARGE SCALE ACCRETION**

The first family of three star particles is shown in Figure ?? and the second family of two star particles is shown in Figure ???. We plot these particles and their surrounding 4×10^{-2} pc region as slices perpendicular to the local angular momentum vector. We determine the local angular momentum vector by taking a 0.01 pc region about the star particle to calculate the angular momentum vector. It is clear from these plots that the clumpy filamentary nature of the local star forming environment extends down to much smaller scales than we have been able to probe in previous work (Lee et al. 2014).

At small radii (similar to 10^{-2} pc), a protostellar disk appears in all five snapshots. The radial size of these disks varies. These disks also show a coherent sense of rotation about a common axis, e.g., no counter-rotating disks. In addition, some of the snapshots show multiple high density regions. This could be a result of accretion of high density clumps or fragmentation in the disk or streams.

We also include a zoom-out picture of the same region, which is the same for all three stars (lower right plot in Figure ??, bottom plot in Figure ??). While this is not unexpected as star formation is clustered, the large scale dynamics are determined by the larger region. We should note that these star particles are within about 0.1 pc of each other in their respective families.

ARE THESE DISK GRAVITATIONALLY

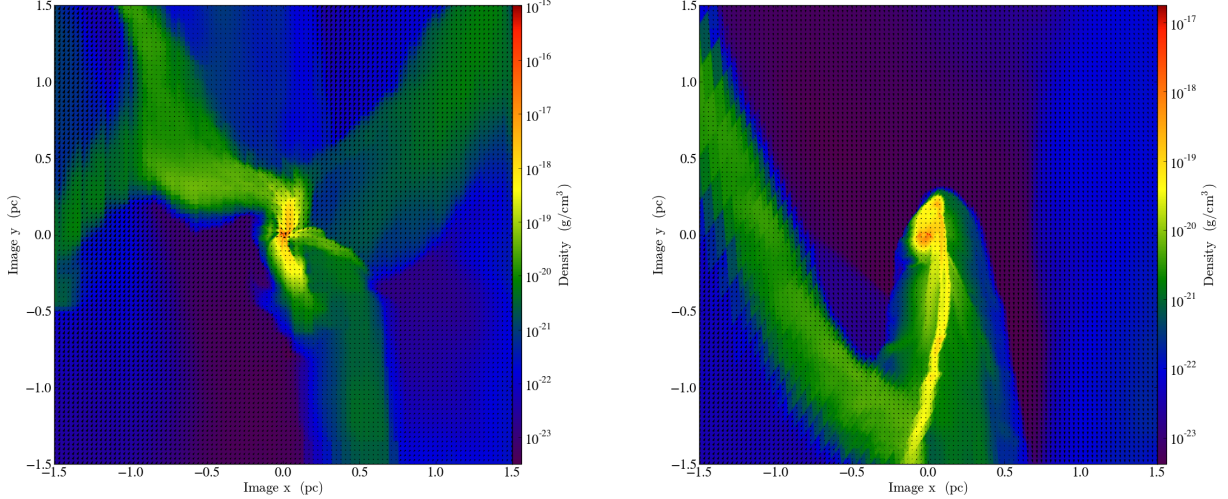


FIG. 2.— Cut of the two star forming regions.

STABLE?

In prior work, we examined the geometry of accretion, i.e., does the accretion proceed along filament or over 4π steradian, by plotting the cumulative accretion rate as a function of density. In Figure ??, we plot the cumulative accretion rate as a function of density, normalized to the average density in shells of radii 0.5 (upper plots) and 0.02 pc (lower plots). Plots on the left are associated with the more massive star forming region, where 3 star particles reside and plots on the right are associated with the less massive star forming region, where two star particles reside. The density where 50% of the accretion is accounted for occurs at $\rho/\bar{\rho} \approx 3$ for the more massive star forming region and appears to be independent of whether the shell has a radius of 0.5 or 0.02 pc. This suggests that the accretion is proceeding along filaments. Similarly, the less massive star forming region has half of the accretion account for at $\rho/\bar{\rho} \approx 10$ at $r=0.5$ pc, again suggesting filamentary accretion. However, this filamentary nature of accretion does not maintain itself to lower radii, where at 0.02 pc, the 50% point in cumulative accretion occurs at $\rho/\bar{\rho} \approx 1$, which suggest accretion is spherical.

Figures ?? and ?? show the moments of inertia for the three star particles in the more massive and less massive star forming regions, respectively. For the more massive star forming region (Fig. ??), note that the moments of inertia are identical for radii greater than $2e-2$, due the fact that these three star particles sit in the same massive star forming region. This is similarly true for the less massive region for $r \gtrsim 0.1$ pc. At small radii, the distribution of gas appears to be flattened or rod-like, which is implied by the relative values of the three principle axes. Around $r \approx 0.02$ and $r \approx 0.1$ pc, respectively, the geometry of the gas is relatively spherical. Outside this region, the gas become flatter again. However, the flattened distributions seen at small and larger radii may also reflect the effect of streams of gas or gravitational instabilities that are associated with the accretion.

3.1. Radial Profile of Collapse

These simulations display much more complicated dynamics than is captured by the simple analytic theory

of Murray and Chang 2014. In spite of this, we proceed to compare radially averaged profiles around these high density points to their analytic theory. Toward this end, we construct radial profiles around the most massive star particle in each of the star forming regions.

In Figure ??, we show the radial distribution of ρ , v_r , v_t , $M(r)$, \dot{M} , and the density distribution function around the three star particles. In the top left plot, we show a slice of the region perpendicular to the z -axis. The top right plot shows $\rho(r)$ alongside lines of $r^{-3/2}$, r^{-2} and $r^{-5/2}$. Here we find that at small radii, $\rho(r) \sim r^{-2}$ at small radii and $\rho(r) \sim r^{-3/2}$ between 0.1 - 1 pc. At other radii, the density profile is surprisingly steep, steeper than even $r^{-5/2}$.

The velocity profiles show similar change in behavior in the transition increasing from small radii, around $r \approx 0.02$ pc. The radial velocity tends to increase to 0.02 pc, and then decreases following the slope noted in the red line of 0.5. This demarcation from the smaller radii to larger is due to the disk-like shape of the star particle at the smaller radii. The turbulent velocity, green line, decreases inward.

The middle right graph shows the mass as a function of radius. The mass monotonically increases. However there is a flattening around 0.1 pc before it steepens again. This is important because this region behaves similarly to a point mass. Which is also reflected in the density profile and the radial velocity profile where $\rho \sim r^{-1.5}$ and $v_r \sim r^{-1/2}$ as shown by MC15 around point masses.

The bottom left graph shows the mass accretion rates for all three particles in the more massive region. At small radii, the drop off in \dot{M} is due to the presence of a disk, the drop off at larger radii is due to the step density profile.

The bottom right graph depicts the density PDF for three different radii. Here it roughly corresponds to the density profile shown in the top right plot. For instance, the PDF inside a 1 pc sphere has a slope of $\rho^{-1.3}$ which corresponds to a radial profile of $\rho \sim r^{-2.5}$, whereas for a 2 pc sphere, the slope is now $\rho^{-1.5}$ corresponding to radial profile of $\rho \sim r^{-2}$.

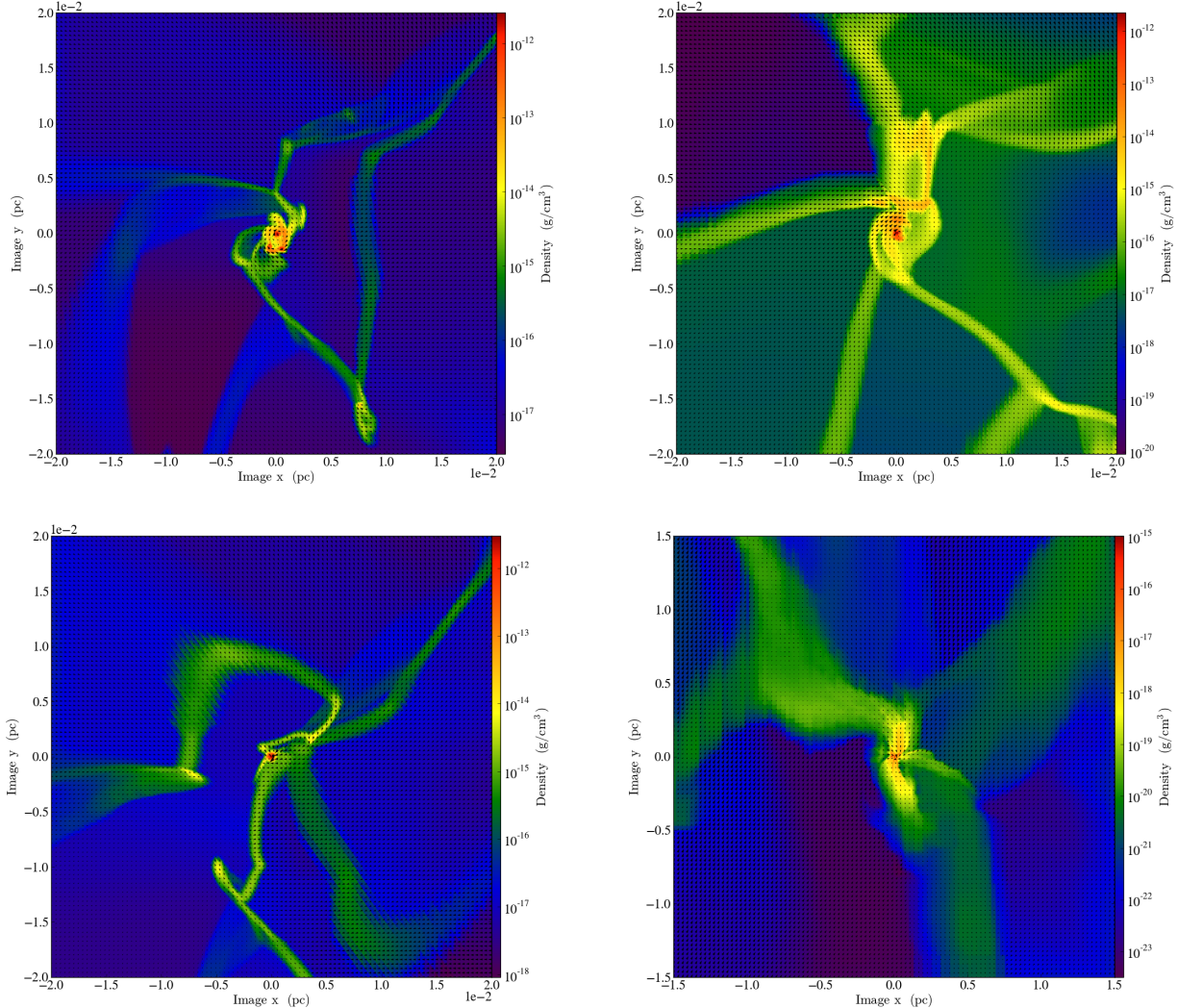


FIG. 3.— The upper frames, and the bottom left frame show slices along the angular momentum axis of three local particles in one of the regions demonstrating significant star formation. Each of the zoomed-in slices have a radius of 0.02 pc. To determine the angular momentum axis, we take a 0.01 pc region about the densest local point and calculate the angular momentum vector. We then take a slice in the plane normal to the angular momentum vector to plot the regions around these dense points. The bottom right frame shows the comparative plots for the less massive region are shown in the upper left graph shows a slice perpendicular to the z axis in the plane of peak density around this region of star formation. The graph shows a single filamentary strand of accretion towards the inner disk-like structure.

Here again the top right plot shows $\rho(r)$ alongside lines of $r^{-3/2}$, r^{-2} and $r^{-5/2}$. Between $0.01 \text{ pc} \lesssim r \lesssim 0.1 \text{ pc}$, ρ closely matches the slope of $r^{-3/2}$. This same region shows a flattening in the mass profile (middle right plot) and a radial velocity profile that is similar to $r^{-1/2}$ (middle left plot). This region also shows flat \dot{M} profile (lower left plot). For larger radii, the density profile shows a break toward a steeper power law in r and the velocity profiles shows a switch to rising with r rather than falling with r . The mass profile shows a continued monotonic increase with r , indicating that the mass is dominated by the gas and not by a central mass.

In addition, a sharp spike in density appears at $r =$

$6e-3 \text{ pc}$ that is notable in the velocity, mass, and \dot{M} plots as well. The plot of moments of inertia also indicate that this point is where the two particles begin to diverge most significantly.

The middle left plot shows the velocity profiles, which also indicate an anomaly at $r \approx 6e-3 \text{ pc}$. However, the general trend of both turbulent and radial velocity is increasing inward from $r \approx 0.1 \text{ pc}$, and also increasing outward from $r \approx 0.1 \text{ pc}$.

The mass distribution, the middle right plot, again increases monotonically. The flattening in this less massive region occurs at the notable radius of $r \approx 6e-3 \text{ pc}$, before steepening again.

3.2. Average Profiles

4. DISCUSSION AND CONCLUSIONS

Write

REFERENCES

- Bethe, H. A. & Salpeter, E. E. 1957 *Quantum Mechanics of One- and Two-Electron Atoms* (Berlin: Springer-Verlag) (BS)

- Bildsten, L., Salpeter, E. E. & Wasserman, I. 1992, ApJ, 384, 143 (BSW)

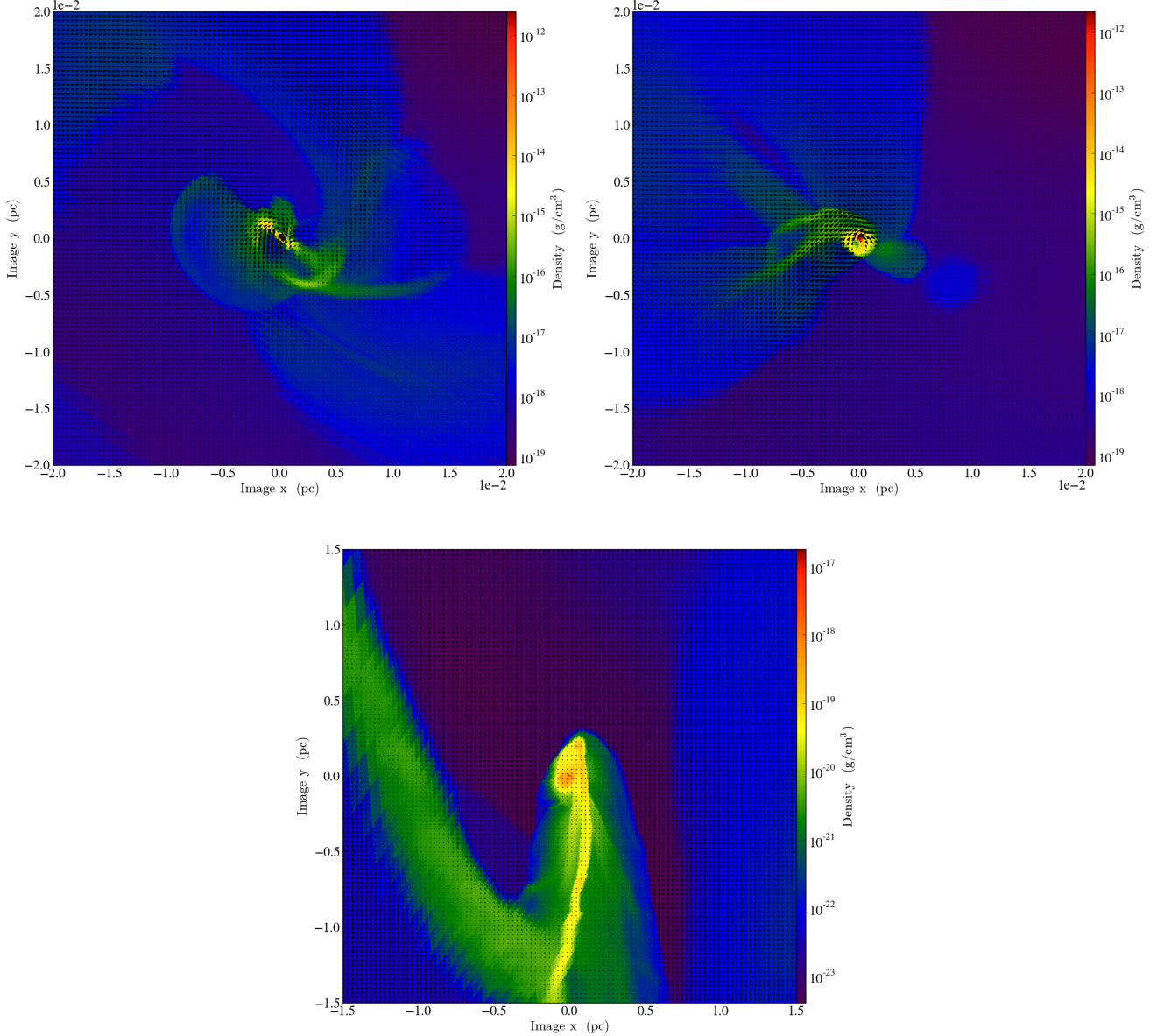


FIG. 4.— The upper frames show the zoomed-in slices along the angular momentum axis of the local particles in the second region of significant star production. Again, each of the zoomed-in slices have a radius of 0.02 pc. The bottom frame shows the zoomed out region, with a radius of 1.5 pc.

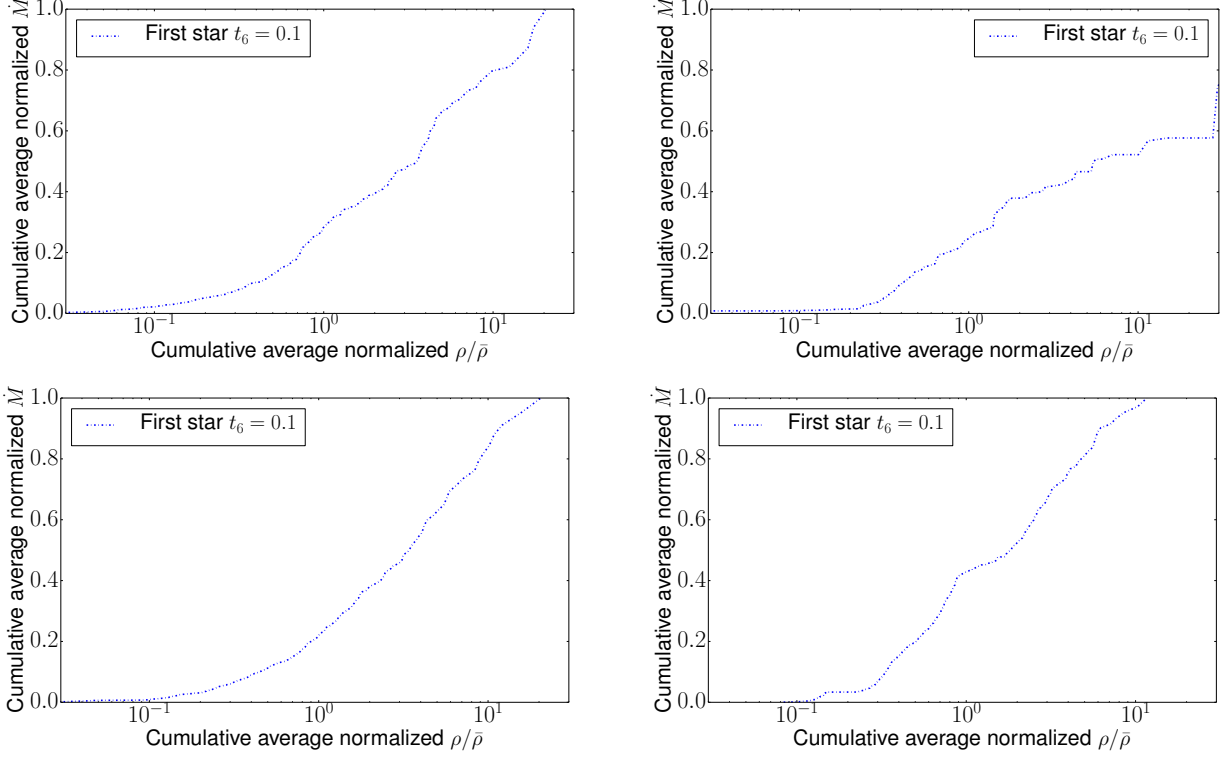


FIG. 5.— Here we show the mass accretion rates as a function of density. The upper figures are displaying rates corresponding to a region of 0.5 pc around the particle, while the lower figures are showing a radius of 0.02 pc. The two plots on the left show the region with three particles forming, and the plots on the right show the region with two particles forming. The more massive region with three particles indicates the mass is coming in at a density value roughly three times the average density, and the curves are similar between the smaller and larger radii. The graph for the less massive region on the right shows a distinctly separate profile between the larger and the smaller radius.

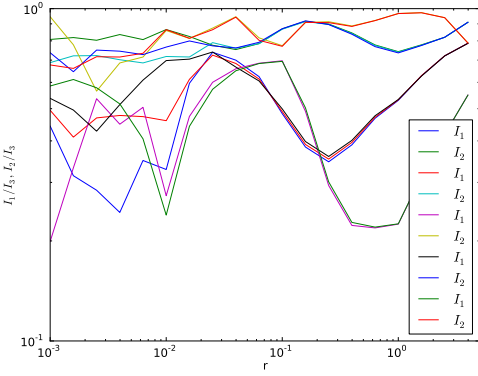


FIG. 6.— Plots of the moments of inertia for the three star particles in the more massive star forming region. Note that the moments of inertia are identical for radii greater than $2e - 2$, due to the fact that these three star particles sit in the same massive star forming region. Inside this region, we find that the two largest moments of inertia are close in value to each other, suggesting that the geometry of the gas resembles a flattened distribution. Around $r \approx 0.02$ pc, the geometry of the gas becomes relatively spherical. Outside this region, the gas become flatter again. However, the flattened distributions seen at small and larger radii may also reflect the effect of streams of gas that might drive the accretion.

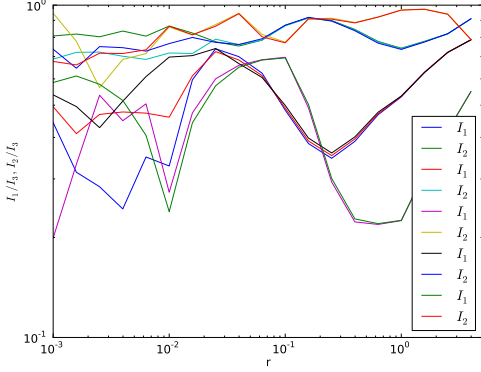


FIG. 7.— *Geometry₂* and *geometry₄* Plots of the moments of inertia for the two star particles in the less massive star forming region. The moments of inertia for these particles are identical down to a radius of $r \approx 0.1$ pc

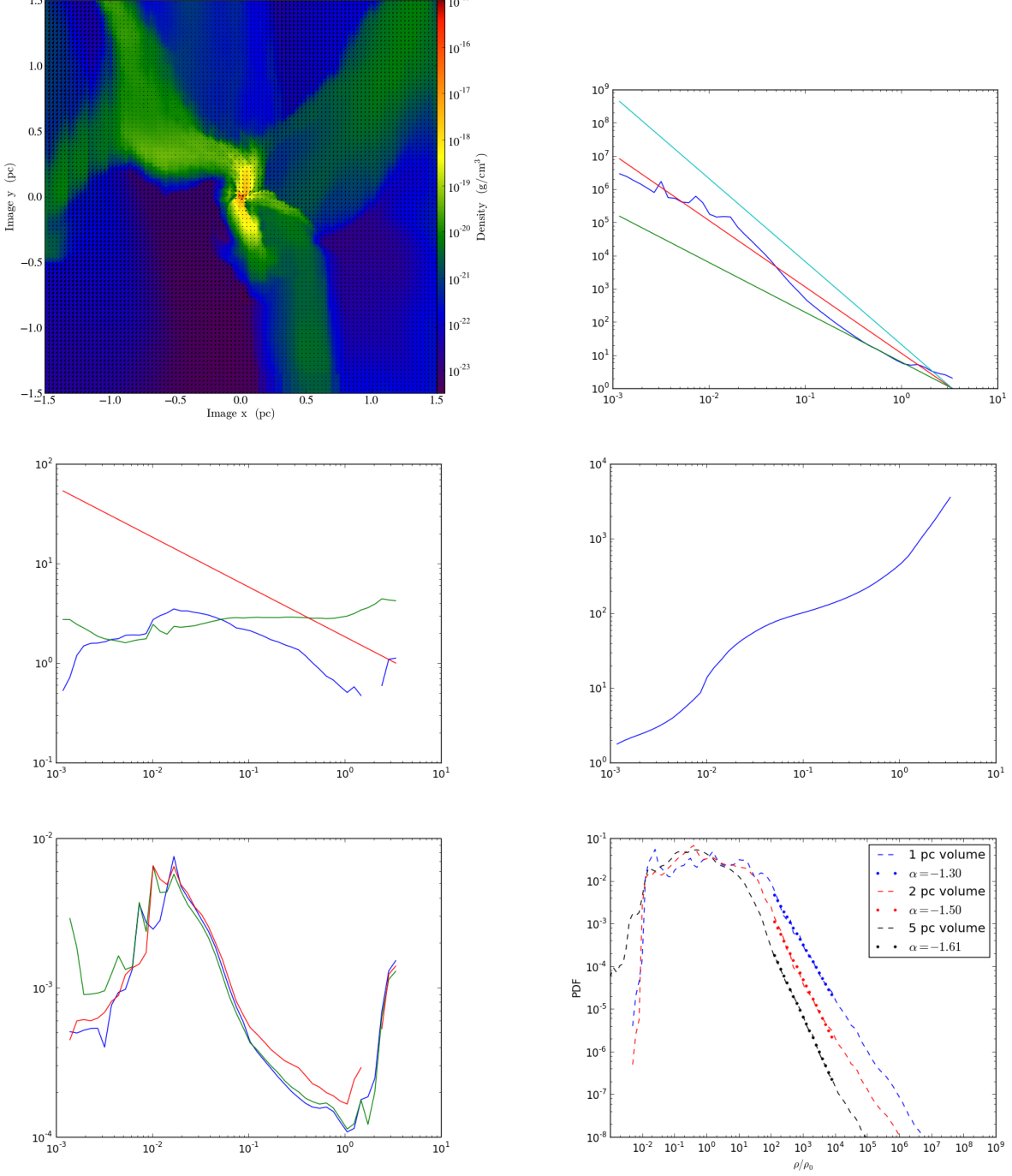


FIG. 8.— Tracking 132 000 These plots show various data for one of the particles formed in the more massive region in the simulation. The upper left plot shows the zoomed out region with radius of 1.5 pc. The upper right graph shows the density profile for one of the particles in the region with reference lines indicating slopes of $-5/2$, -2 , and $-3/2$. The slope between 0.02pc and 0.4pc approximately matches the $-5/2$ reference line. The middle left shows a plot of the radial velocity and turbulent velocity associated with the particle. The middle right graph shows the radial density profile of the particle. The plot on the lower left compares the mass accretion rates between the three particles in the more massive region. The accretion rates are very similar at radii greater than $r \approx 10^{-2} \text{ pc}$. The plot on the lower right shows the pdf function related to volumes of 1pc, 2pc, and 5pc.

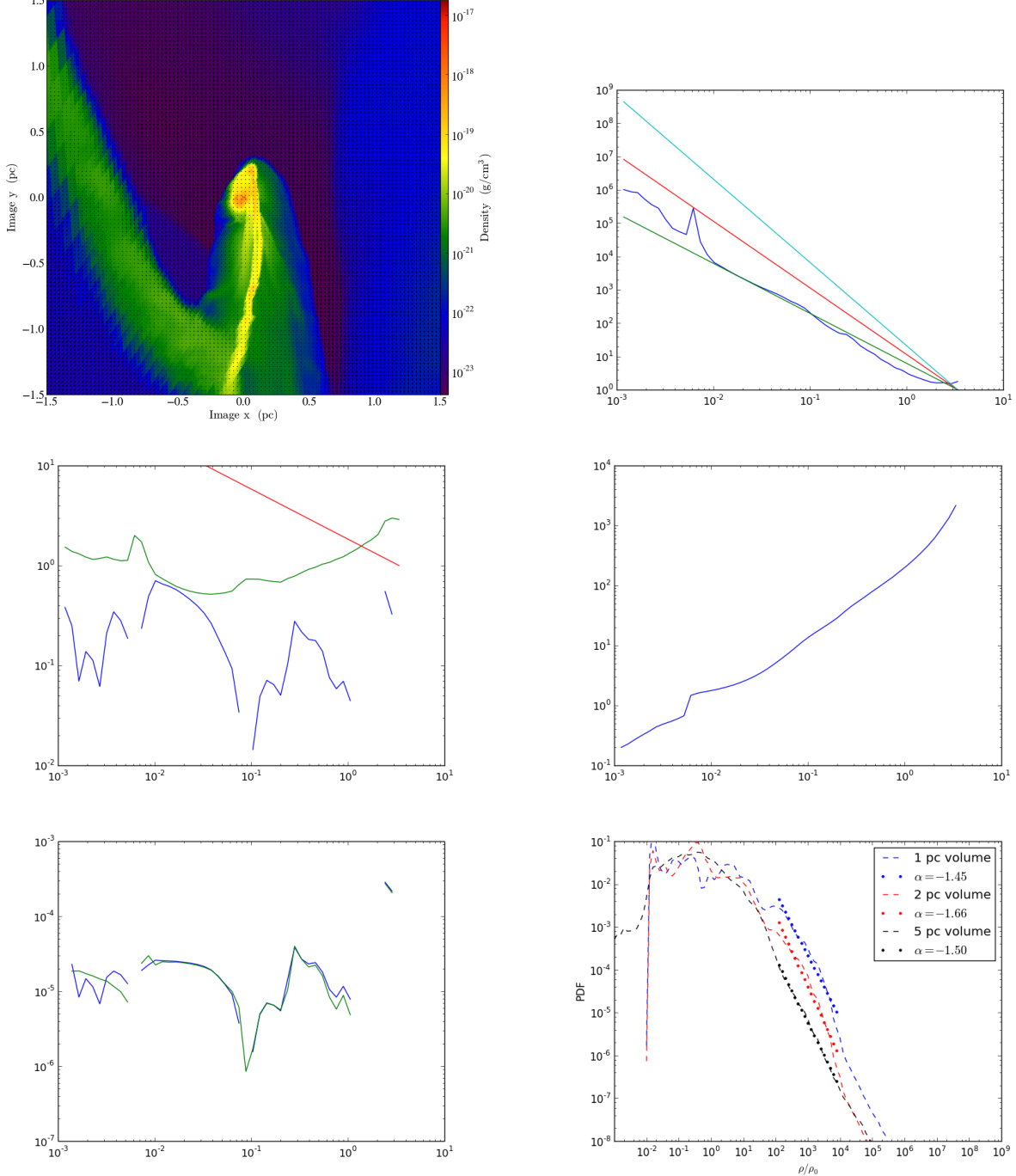


FIG. 9.— Tracking 132 002 These plots show the data for a different particle formed in the simulation at the same time as the previous plots. The upper left graph of the density in the region neatly matches the $-3/2$ slope. The pdf graph in the upper right again shows the plots for volumes related to 1pc, 2pc, and 5pc. The lower left plot demonstrates the loose connection between the radial velocity and the turbulent velocity. The graph on the lower right again shows the density profile of this second particle.

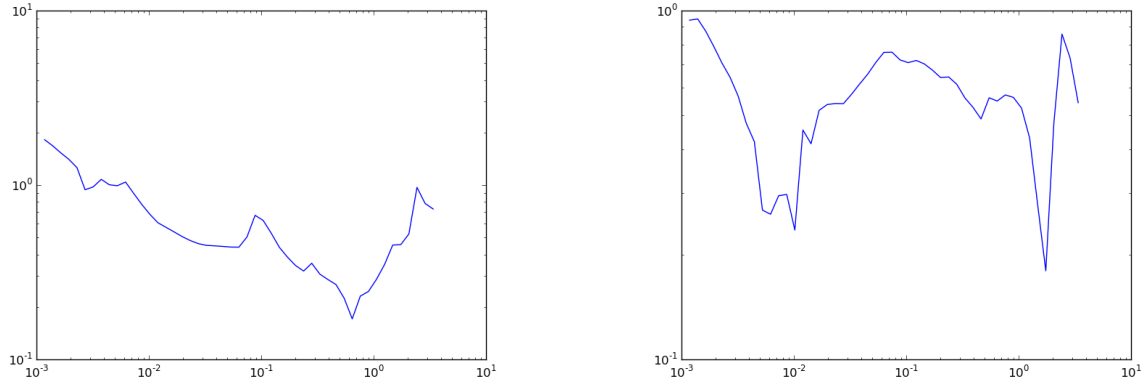


FIG. 10.— WRITE CAPTION: Angular momentum as a function of distance from maximum density point.